2016

Intermittency of Gravity Wave Momentum Flux in the Mesopause Region Observed with an All-Sky Airglow Imager

Bing Cao

Alan Z. Liu
Embry Riddle Aeronautical University, liuz2@erau.edu

AGU PUBLICATIONS

JGR

Journal of Geophysical Research: Atmospheres

RESEARCH ARTICLE
10.1002/2015JD023802

Key Points:
- Gravity wave intermittency in the mesopause region is higher over the Pacific than over the Andes
- The pdf of GW momentum flux follows piecewise lognormal and power law functions
- The background variations are likely a main contributor to GW intermittency in the mesopause

Correspondence to:
B. Cao,
caob@my.erau.edu

Citation:
Cao, B., and A. Z. Liu (2016), Intermittency of gravity wave momentum flux in the mesopause region observed with an all-sky airglow imager, *J. Geophys. Res. Atmos.*, *121*, doi:10.1002/2015JD023802.

Received 15 JUN 2015
Accepted 11 DEC 2015
Accepted article online 23 DEC 2015

Intermittency of gravity wave momentum flux in the mesopause region observed with an all-sky airglow imager

Bing Cao[1] and Alan Z. Liu[1]

[1]Center for Space and Atmospheric Research, Department of Physical Sciences, Embry-Riddle Aeronautical University, Daytona Beach, Florida, USA

Abstract The intermittency of gravity wave momentum flux (MF) near the OH airglow layer (~87 km) in the mesopause region is investigated for the first time using observation of all-sky airglow imager over Maui, Hawaii (20.7°N, 156.3°W), and Cerro Pachón, Chile (30.3°S, 70.7°W). At both sites, the probability density function (pdf) of gravity wave MF shows two distinct distributions depending on the magnitude of the MF. For MF smaller (larger) than ~16 m^2 s^{-2} (0.091 mPa), the pdf follows a lognormal (power law) distribution. The intermittency represented by the Bernoulli proxy and the percentile ratio shows that gravity waves have higher intermittency at Maui than at Cerro Pachón, suggesting more intermittent background variation above Maui. It is found that most of the MF is contributed by waves that occur very infrequently. But waves that individually contribute little MF are also important because of their higher occurrence frequencies. The peak contribution is from waves with MF around ~2.2 m^2 s^{-2} at Cerro Pachón and ~5.5 m^2 s^{-2} at Maui. Seasonal variations of the pdf and intermittency imply that the background atmosphere has larger influence on the observed intermittency in the mesopause region.

1. Introduction

Atmospheric gravity waves (GWs) are ubiquitous in the atmosphere. As these waves propagate upward to the mesosphere and lower thermosphere (MLT) region, most of them dissipate due to either critical level filtering or instabilities when waves reach large enough amplitudes and deposit momentum and energy into the background atmosphere. This process has significant impacts on the global circulation and thermal balance by forcing the global-scale Brewer-Dobson meridional circulation, which leads to a dynamical balance rather than radiative balance in the middle atmosphere [*Butchart*, 2014; *Cohen et al.*, 2014; *Gierasch et al.*, 1970; *Andrews et al.*, 1987; *Liou*, 2002].

GWs with different characteristics appear with different probabilities in the atmosphere due to the random nature of both GW generation and the variation of the background atmosphere they propagate through. Convection and topography are two important sources of gravity waves. Convective GWs show significant temporal variability and are also spatially localized [*Fritts and Alexander*, 2003; *Alexander et al.*, 1995, 2004]. Orographic GWs are directly related to the flow over the topography of mountain ridges or islands in the ocean. The randomness of the low-level winds thus contributes to the intermittency of GWs. As a result, GW dissipation and forcing on the atmosphere are random and often highly intermittent. The extremely large GW forcing associated with breaking of large amplitude GWs can alter the background atmosphere significantly, even though these waves may happen rarely and their long-term effect may be small. On the other hand, small-amplitude GWs are more ubiquitous. Even though their short-term effects are small, they could have a lasting impact on the background atmosphere. In order to understand the comprehensive effects of GWs in the atmosphere, both the long-term mean properties of GWs and the effects of a minority of large GWs need to be studied.

Most general circulation models (GCMs), due to coarse resolutions, cannot resolve small-scale GWs and have to resort to parameterizations to include their effects on the background atmosphere [*Fritts and Alexander*, 2003; *Beres et al.*, 2005; *Richter et al.*, 2010]. In these parameterizations, an "intermittency" parameter is needed to describe the fraction of time and space of the presence of GWs over a long period of time and within a

large area. This parameter is tuned to make the average GW forcing more realistic [*Alexander and Dunkerton*, 1999; *Fritts and Alexander*, 2003]. In Lindzen-type parameterization [*Lindzen*, 1981], which treats each GW independently based on linear GW theory, the "efficiency factor" reflects some basic ideas of intermittency. It is found that a fairly small value of this factor (~0.1) is suitable to produce realistic simulations [*Holton*, 1982]. *Alexander and Dunkerton* [1999] define a formula for intermittency for the GWs source as the ratio of the average of momentum flux (MF) in active time to its long-term average. The importance of the intermittency parameter, especially in the parameterization of orographic GW drag, is discussed in detail in *Alexander et al.* [2010]. A parameterization needs to specify proper GW amplitude (or MF) so they break at the correct altitudes. In the meantime, parameterized GWs have to provide proper magnitude of the forcing so the model can produce realistic mean zonal wind. The latter is achieved by tuning the intermittency parameter.

Recently, *Hertzog et al.* [2012] and *Plougonven et al.* [2013] investigated the intermittency of GW MF in the lower stratosphere above Antarctica and the Southern Ocean using balloon data. They found that the probability density functions (pdfs) of GW MF largely follow a lognormal distribution and some deviation from lognormal distribution is found at the larger MF. Monte Carlo simulations were used to show that the lognormal distribution can be explained by the random nature of the background wind variation which affects the critical level filtering. Similar analysis has been done by *Wright et al.* [2013] on a global scale using HIRDLS satellite data for GWs in the 25–65 km altitude. These works based on different data reveal several important facts about GW intermittency: The intermittency of GW MF in the stratosphere varies with season and altitude; the intermittency over mountain areas is significantly higher than in other areas, represented by a longer tail in pdfs of GW MF; and those rare waves with extremely large MF contribute significantly to the total MF.

In this study, the intermittency of GW MF in the mesopause region, where GW breaking and dissipation are strongest, is investigated for the first time. The analysis is based on a large number of GWs identified from multiyear OH airglow measurement (around 87 km altitude) at Maui, Hawaii (20.7°N, 156.3°W), and at the Andes Lidar Observatory (ALO) in Cerro Pachón, Chile (30.3°S, 70.7°W). We focus on the statistical characteristics, in particular the pdfs of GW MF at these two sites with distinctively different GW sources. Maui is in the middle of the Pacific with no nearby strong GW sources, while ALO is in the Andes Mountains with strong orographic GW sources. We compare the results of these two sites to examine the differences in intermittency that may be attributable to the differences in wave source and background atmosphere. Based on the pdfs, we also compare the relative importance of GWs with large and small MFs.

In the next section we describe the instrument, data set, and analysis methods used to obtain the pdfs. Section 3 presents the pdfs of GW MF at Maui and Cerro Pachón, the intermittency measures based on three diagnostic parameters, comparison of the relative importance of waves with large and small MFs, and the seasonal variations of pdfs and intermittency. The significance of these findings are discussed in section 4, followed with conclusion in section 5.

2. Data and Methodology

An all-sky airglow imager was deployed in Maui as part of the Maui Mesosphere and Lower Thermosphere (Maui MALT) campaign from January 2002 to August 2007 and was later relocated to ALO in Cerro Pachón, Chile, in September 2009. The imager took all-sky images of OH airglow emission at night during the low Moon periods throughout the year. High-frequency, quasi-monochromatic GWs are identified from these images using a series of procedures described in detail by *Tang et al.* [2002, 2005a, 2005b]. This method was applied to the Maui imager data to study the seasonal variation of GW MF [*Tang et al.*, 2005c] and the characteristics of GW intrinsic parameters [*Li et al.*, 2011]. Similar procedures were used in *Suzuki et al.* [2009] to study the equatorial GWs. A 2-D spectral method is used to identify GWs from airglow images. Three consecutive images were used to form two consecutive time-difference (TD) images for spectral analysis. Intrinsic wave parameters including wavelength, phase speed, propagation direction, and relative airglow intensity perturbation ($I'_{OH}/\bar{I}_{OH}$) were derived from each set of two TD images, with the background winds provided by a collocated meteor radar [*Franke et al.*, 2005]. The GW MF was calculated based on their intrinsic parameters and the temperature amplitude, converted from $I'_{OH}/\bar{I}_{OH}$ using the airglow model described in *Swenson and Gardner* [1998] and *Liu and Swenson* [2003]. For each set of two TD images, there can be zero to multiple GWs identified and counted. The total number of identified GWs is listed in Table 1, together with the number of nights that imager data are available. As revealed in *Li et al.* [2011], most of the GWs identified with this method are high frequency with periods less than 30 min and small scale with horizontal wavelength shorter than 120 km. The results of this study therefore apply to GWs

Table 1. Statistics of Wave Measurements at Maui and Cerro Pachón

Location	Start Date	End Date	Total Nights	Number of Waves[a]
Maui	2002/5/20	2007/6/13	591	12079
Cerro Pachón	2009/9/20	2012/11/10	219	60409

[a]See the definition in the text.

in this parameters range only. While lower frequency, larger horizontal-scale GWs are not included, they are expected to be less frequent in the mesopause region and carry less MF [*Fritts and Vincent*, 1987].

While the instrument and algorithm for identifying GWs for the two sites are the same, there are two notable differences. First, the Milky Way over Cerro Pachón is present and close to zenith most of the time and is much brighter than airglow emission within the imager observation bandwidth. An additional procedure of removing the Milky Way [*Li et al.*, 2014] is necessary and applied before GWs are identified. Second, the exposure time of each image was 2 min at Maui and 1 min at Cerro Pachón. The longer exposure time in Maui has little influence on the sensitivity to GW detection because most of the GW periods are longer than 5 min. The difference in temporal resolution largely contributes to the larger numbers of GWs identified at Cerro Pachón than that at Maui as shown in Table 1. Better sky conditions at Cerro Pachón are also a contributing factor.

The pdfs of the MF are calculated from the whole data set for each site. For MF values up to 200 $m^2\ s^{-2}$, we divide them into small bins and counted the number of waves in each bin, then divided it by the total number of waves, to obtain the occurrence frequency. Since the occurrence frequencies have extremely large dynamic range, varying 3–4 orders of magnitude from the smallest to the largest MF values, the bin size of MF is chosen to be uniform at logarithmic scale. As such, the actual bin size is smaller for smaller MF values and increases with the MF value. This approach is similar to that used by *Wright et al.* [2013] in order to obtain a more reliable estimate of the probability at large MF values. The occurrence frequency in each bin was then normalized by the bin width, so the final pdfs were obtained in unit of probability per unit MF, i.e., $m^{-2}\ s^2$.

It is important to note that when a wave is identified in a set of two TD images (a group of three consecutive images), it is counted as one wave. If a wave event lasted over multiple sets of TD images, one wave was identified from each set so multiple waves were recorded. Therefore, the number of waves defined in this study is not the number of coherent "wave events"; rather, it is a quantity proportional to the duration of waves. With this definition, the number of waves within a MF range reflects the probability of waves within this range, and the total MF can be obtained as the sum of the products of the MF values and their probabilities. Another consequence of this image analysis approach is that the TD images automatically exclude stationary features such as mountain waves, which could be very strong at Cerro Pachón. The implication of this is discussed in more detail in section 4.

3. Results

3.1. Probability Density Function

Figure 1 shows the pdfs of the absolute MF ($\sqrt{\langle u'w'\rangle^2 + \langle v'w'\rangle^2}$) at Maui and Cerro Pachón for the whole data set. The MF derived from the airglow imager data is $\langle u'w'\rangle$ and $\langle v'w'\rangle$ in unit of $m^2\ s^{-2}$. For easier comparison with other studies, the corresponding values of $\rho\sqrt{\langle u'w'\rangle^2 + \langle v'w'\rangle^2}$ in unit of pascals are also indicated with a second axis in Figure 1, calculated using the mean atmospheric density $\rho = 5.67 \times 10^{-6}$ kg m^{-3} at ~87 km altitude according to NRLMSISE-00 model [*Picone et al.*, 2002]. The latter MF is conserved throughout the altitudes when GWs do not experience dissipation.

Note that the uniform bin size in logarithm scale corresponds to a bin size of ~10 $m^2\ s^{-2}$ at 200 $m^2\ s^{-2}$ and ~0.1 $m^2\ s^{-2}$ at 1 $m^2\ s^{-2}$. The pdfs of both sites show some similarity in their shapes with clear peaks near 1–2 $m^2\ s^{-2}$ and long tails beyond ~10 $m^2\ s^{-2}$. The shape of pdfs shows that there are more GWs with smaller MF at Cerro Pachón than at Maui. And there is relatively less probability of large amplitude GWs at Cerro Pachón. Close examinations of the pdfs suggest that they follow a lognormal function in the small MF range and a power law function in large MF range, with the transition near ~16 $m^2\ s^{-2}$ at both sites.

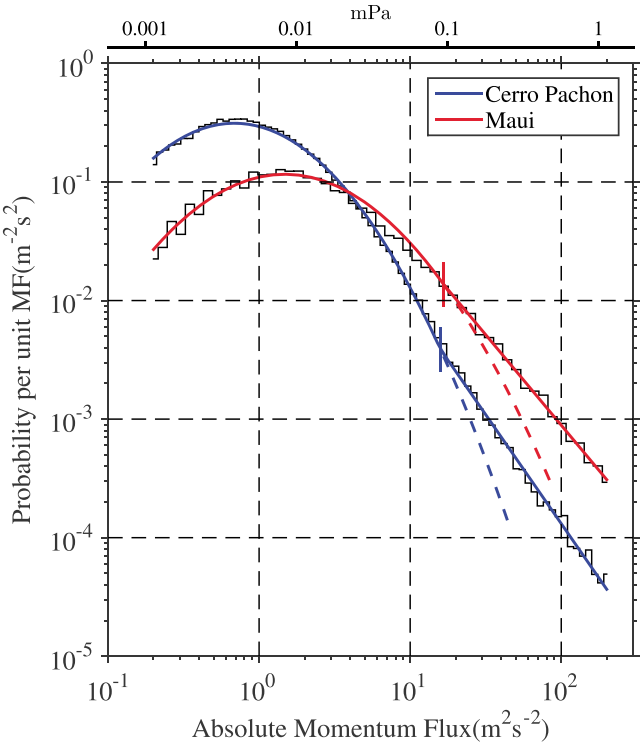

Figure 1. Histograms of the absolute MF from Maui (red) and Cerro Pachón (blue) in the log-log coordinates. Thick solid curves are pdfs based on the least squares fitting of the histograms. The two short vertical lines near 16 m^2 s^{-2} indicate the transition points between the lognormal distribution on the left and power law distribution on the right. The dashed lines are the extensions of the lognormal functions to show the departure from this distribution at large MF. The horizontal axis is absolute MF, with the bottom axis labeled in unit of m^2 s^{-2} and the top axis labeled in unit of mPa.

To obtain analytical expressions of the pdfs, we performed a least squares fit with the following piecewise function:

$$y = \begin{cases} \frac{1}{\sqrt{2\pi}\sigma x} \exp\left(-\frac{(\ln x-\mu)^2}{2\sigma^2}\right) & \text{if } x \le x_0, \\ a\left(\frac{x}{x_0}\right)^b & \text{if } x \ge x_0, \end{cases} \tag{1}$$

of which x is the absolute MF, y is the corresponding probability density, and x_0 is the transition point between the lognormal and power law functions. Continuity between two functions at x_0 is a constraint in the fitting process; i.e.,

$$\frac{1}{\sqrt{2\pi}\sigma x_0} \exp\left(-\frac{(\ln x_0 - \mu)^2}{2\sigma^2}\right) = a. \tag{2}$$

The fitting was done in log-log space, so the result is not overly weighted by the large probabilities at small MF. In log-log coordinates, the function in (1) can be written as

$$\ln y = \begin{cases} -\ln(\sqrt{2\pi}\sigma) - \ln x - \frac{(\ln x-\mu)^2}{2\sigma^2} & \text{if } \ln x \le \ln x_0, \\ \ln a + b(\ln x - \ln x_0) & \text{if } \ln x \ge \ln x_0, \end{cases} \tag{3}$$

so $\ln y$ is a parabolic and a linear function of $\ln x$ in the two regions, respectively. Therefore, instead of fitting the lognormal and power law functions directly, we fit the piecewise function of a parabola and a straight line, with the continuity requirement at the transition point, to obtain values of x_0, μ, σ, a, and b.

Table 2. The Fitted Parameters of the Piecewise Functions at Maui and Cerro Pachón, the Percentages of Waves Included in Each Region, and Their Relative Contributions to the Total MF

	Lognormal				Transition	Power Law			
Location	μ	σ	GW	MF	x_0	a	b	GW	MF
Maui	1.76	1.17	71.3%	18.2%	16.6	0.0137	−1.53	28.7%	81.8%
Cerro Pachón	0.75	1.06	94.0%	48.6%	15.9	0.00388	−1.84	6.0%	51.4%

The pdf parameter values from the least squares fit for Maui and Cerro Pachón are listed in the Table 2. For the lognormal distribution, μ is the mean and σ is the standard deviation of the normally distributed $\ln x$. The mean value μ is much larger at Maui, corresponding to MF = exp(1.76) = 5.8 m^2 s^{-2}, compared with MF = exp(0.75) = 2.1 m^2 s^{-2} at Cerro Pachón. This indicates that the MF is on average larger at Maui. The standard deviations σ are similar at the two sites. The peak of the pdf is located at $\exp(\mu - \sigma^2)$, which is 0.69 m^2 s^{-2} at Cerro Pachón and 1.48 m^2 s^{-2} at Maui. The transition points x_0 are very close at the two sites, around 16 m^2 s^{-2}. For the power law distribution, the magnitude of the slope b is slightly larger at Cerro Pachón, indicating a faster decrease of probability of GWs with larger MF. The fitted piecewise functions are plotted in Figure 1, and they match the probability histograms very well at both sites. Also listed in Table 2 are the fractions of waves included in the lognormal and power law regions of pdf functions and their relative contributions to the total MF. It is clear that most of the waves (71.5% at Maui and 94.0% at Cerro Pachón) are in the lognormal region where MF is relatively small, but waves in the power law region where MF is large contribute more (81.8% at Maui and 51.4% at Cerro Pachón) to the total MF.

The lognormal distribution in GW MF has also been found in the lower atmosphere with satellite [*Alexander and Grimsdell*, 2013; *Wright et al.*, 2013] and balloon [*Hertzog et al.*, 2012; *Jewtoukoff et al.*, 2013; *Plougonven et al.*, 2013] measurements. In these studies, the left side of the lognormal distribution, i.e., the decrease of probability toward smaller MF values, were not clearly shown [see *Hertzog et al.*, 2012, Figure 2; *Alexander and Grimsdell*, 2013, Figure 8; *Jewtoukoff et al.*, 2013, Figure 16]. This makes it difficult to make a proper fit of the lognormal distribution and identify its peak. In Figure 1, a more complete picture of the lognormal distribution is shown with the excellent fit of the probability histograms at both sides of the peak. In the large MF region, the broader tail was noted by *Hertzog et al.* [2012] and *Alexander and Grimsdell* [2013], and *Wright et al.* [2013] suggested some linear relation in log-log scale of the pdfs. We are able to confirm that the long tail region indeed follows a power law function as shown by the straight line in Figure 1 . This power law distribution gives a broader tail (slower decrease with increasing MF) than the lognormal distribution at the large MF region. It indicates that GWs with MF larger than x_0 occur more frequently than a lognormal distribution would imply. *Hertzog et al.* [2012] attributed this broader tail to higher GW intermittency. In the next section, we will study the intermittency in more detail.

Comparison of the MF in unit of pascals shows that the magnitudes of the GW MF (up to 1 mPa) in MLT region are much smaller than those measured in the lower atmosphere (up to 60 mPa in *Hertzog et al.* [2012]). This is expected since the saturation and breaking of GWs restrict the growth of wave amplitudes when they propagate upward. The GWs detected by the airglow imager in the mesopause region, if originated in the lower atmosphere, must have extremely small amplitudes that are not observable there. Alternatively, some of these GWs may be generated in the middle atmosphere through secondary wave generation [e.g., *Snively and Pasko*, 2003; *Vadas et al.*, 2003; *Fritts et al.*, 2009].

3.2. Intermittency

Several parameters, such as the Bernoulli proxy and the percentile ratio used in *Hertzog et al.* [2008], and the Gini coefficient [*Plougonven et al.*, 2013; *Wright et al.*, 2013] have been proposed to quantify the overall intermittency of the GW MF. The Bernoulli proxy is calculated as

$$\epsilon_1 = \frac{1}{1 + \sigma^{*2}/\mu^{*2}}, \tag{4}$$

where μ^* and σ^* are the mean and standard deviation of all MF measurements, respectively. Note that μ^* and σ^* are different from μ and σ in (1). The percentile ratio is defined as a ratio of two percentiles (50% and 90%) of

Table 3. The Three Intermittency Parameters at Maui and Cerro Pachón

Location	Percentile Ratio[a]	Bernoulli Proxy	Gini Coefficient
Maui	0.114	0.738	0.681
Cerro Pachón	0.198	0.878	0.694

[a]The two percentiles are chosen as the 50% and 90%.

MF magnitudes. If a total of N waves are sorted according to their MF magnitude f_i $(1 \le i \le N)$ so $f_{i-1} < f_i$ for all i, the percentile ratio is calculated as

$$\epsilon_2 = \frac{f_{0.5N}}{f_{0.9N}}. \tag{5}$$

Hertzog et al. [2008] explained that for these two parameters, values close to 1 indicate continuous occurrence (low intermittency) and values close to 0 indicate large variability or large intermittency.

Following *Plougonven et al.* [2013], the Gini coefficient is defined as

$$\epsilon_3 = \frac{\sum_{n=1}^{N-1} (n\mu^* - F_n)}{\sum_{n=1}^{N-1} n\mu^*}, \tag{6}$$

where $F_n = \sum_{i=1}^{n} f_i$ is the cumulative sum of MF. It is widely used in economics to describe the inequality of wealth. $\epsilon_3 = 0$ corresponds to perfect equality and $\epsilon_3 = 1$ to total inequality. When applied to the intermittency, a large (small) Gini coefficient corresponds to large (small) intermittency, opposite to that represented by ϵ_1 and ϵ_2 .

Here we use all three parameters to assess the intermittency of GWs from the airglow data. As shown in Table 3, the Bernoulli proxy and the percentile ratio both indicate that GWs at Maui have larger intermittency, while the Gini coefficient shows no significant difference. In *Plougonven et al.* [2013], the average Gini coefficients calculated from balloon observations in the stratosphere (17–19 km altitude) vary from 0.44 over the Southern Ocean to 0.63 over the Antarctic Peninsula. The difference is attributed to the difference between orographic and nonorographic GW sources. The Gini coefficients calculated from the HIRDLS data (25–65 km altitude) are less than 0.4 in all regions with some variations with respect to altitude from the stratosphere to the lower mesosphere [*Wright et al.*, 2013]. Our Gini coefficients at both sites are larger than these lower atmospheric values, indicating higher intermittency in the mesopause region.

The difference in the intermittency measures from the three parameters suggests that there may not be a single best parameter to measure the observed GW intermittency. Bernoulli process treats the GW source as two simple "on" and "off" processes without varying amplitude and, therefore, is too simple to reflect the realistic sources with varying amplitudes. The percentile ratio largely depends on two arbitrarily chosen percentiles and cannot adequately represent the whole probability distribution. In addition, as shown in section 3.1, the observed pdfs cannot be represented with a single function. To quantify the relationships between the shape of a pdf and the intermittency measures, we performed Monte Carlo simulations with randomly generated MF values that satisfy a given pdf and calculated the three intermittency parameters from these MF values to examine how they vary with the pdf shape. The pdf parameters σ and μ vary in the range of 0.1 ~3.0, which includes our fitted values. The slope b and the transition point x_0 are fixed using the fitted values at Maui and Cerro Pachón. Figures 2a–2c (Figures 2d–2f) show the variations of the three intermittency parameters as functions of μ (σ), with σ (μ) fixed using the values at the two sites. The intermittency parameters calculated from the airglow measurements are indicated by crosses.

Figure 2 shows that the percentile ratio and the Gini coefficient are generally consistent, as their values vary with opposite trends (same trends in intermittency) as functions of μ as well as σ. However, the percentile ratio and the Bernoulli proxy are not always consistent. Comparing the percentile ratio with the Bernoulli proxy as functions of μ, we can see that they both indicate an increase in intermittency (decrease in parameter values) as μ increases up to 1.5. However, their trends are opposite when $\mu > 1.5$. For variations with σ, again they vary in opposite direction for $\sigma < 1.0$. Therefore, the two intermittency parameters may give opposite change

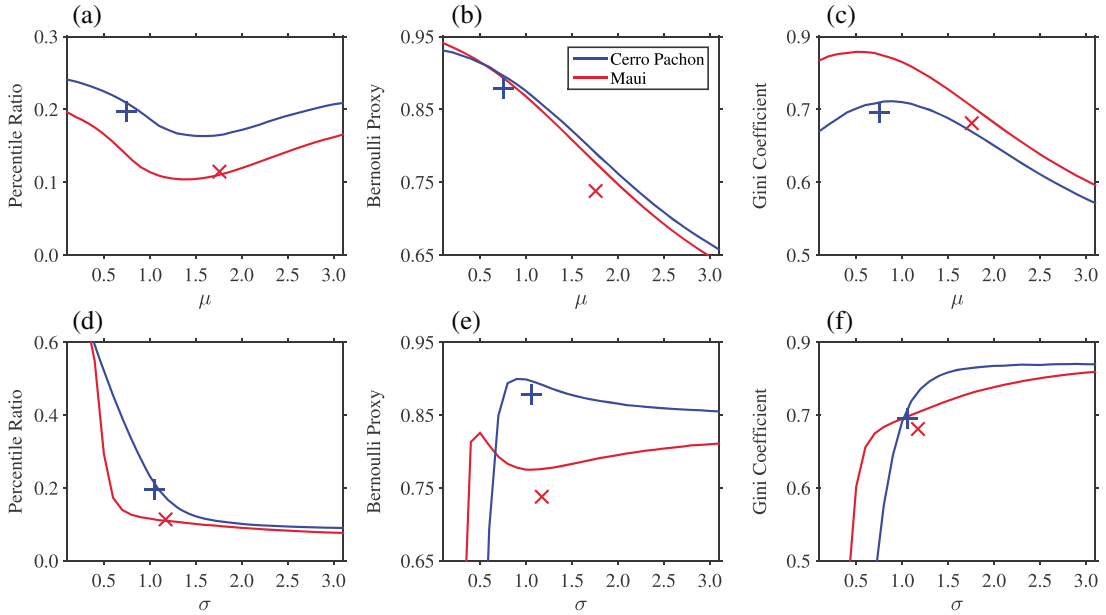

Figure 2. The intermittency parameters as functions of (a–c) μ or (d–f) σ. In Figures 2a–2c (Figures 2d–2f), σ (μ) and b values are fixed using the fitted values in Table 3 at the two sites. Crosses in the plots mark the fitted pdf parameters. The percentile ratio (Figures 2a and 2d), Bernoulli proxy (Figures 2b and 2e), and Gini coefficient (Figures 2c and 2f) are calculated with Monte Carlo simulations.

in intermittency with the same change in pdf. These inconsistencies show that one needs to be careful when using these parameters to measure the intermittency.

3.3. Relative Importance of Large and Small Waves

From the pdfs, it is clear that GWs with small MF occur much more frequently than those with large MF. When GWs break and deposit momentum to the background atmosphere, their impact is related to the total momentum flux, i.e., the product of MF magnitudes and the durations of the waves. To compare quantitatively the relative contributions of GWs with different MF values, we make use of the Lorenz curve [*Lorenz*, 1905], which, like Gini coefficient, is also used in economics to represent wealth distribution.

We first sorted all detected GWs according to their MF magnitudes and then calculated the cumulative MF as a function of the fraction of waves. This is shown in Figure 3a. A point $(x = n/N, y = F_n/F_N)$ on the curve indicates that the bottom x fraction of waves (ranked according to their MF magnitude) contribute y fraction to the total MF. When the Lorenz curve is a straight diagonal line, the MF contribution is evenly distributed among all waves. The Gini coefficient is represented as the ratio of the area between this diagonal line and the observed Lorenz curve to the total area below this diagonal line. The closer the curve to the diagonal line, the more uniform the distribution is and thus less intermittency.

A feature to note in Figure 3a is that the two Lorenz curves for Cerro Pachón and Maui intersect. The cross point corresponds to 78% percentile of GWs at 25% total MF contribution. Because of the crossing of the two curves, the areas between the curves and the diagonal line are similar for the two sites, leading to the close Gini coefficients. This is an evidence that the Gini coefficient is sometimes insufficient to describe the overall MF distribution.

For Maui, the intersection point of the two Lorenz curves corresponds to MF of 23.5 $m^2\ s^{-2}$. This value is about 4 times the mean value in the lognormal region (5.8 $m^2\ s^{-2}$, see section 3.1) and is well beyond the transition point $x_0 = 16.6\ m^2\ s^{-2}$. Therefore, the contribution to the total MF at Maui is mainly from GWs in the power law region with very large MF values, which are highly intermittent. One example of such a large MF wave at Maui was reported by *Li et al.* [2007] based on both airglow imager and Na lidar measurements, in which case the MF was about 70 $m^2\ s^{-2}$. For Cerro Pachón, the intersection point corresponds to MF of 4.9 $m^2\ s^{-2}$, a little over twice the mean value of 2.1 $m^2\ s^{-2}$ in the lognormal region and is much less than the transition point $x_0 = 15.9\ m^2\ s^{-2}$. Therefore, at Cerro Pachón a significant portion of the total MF is from GWs with small MF.

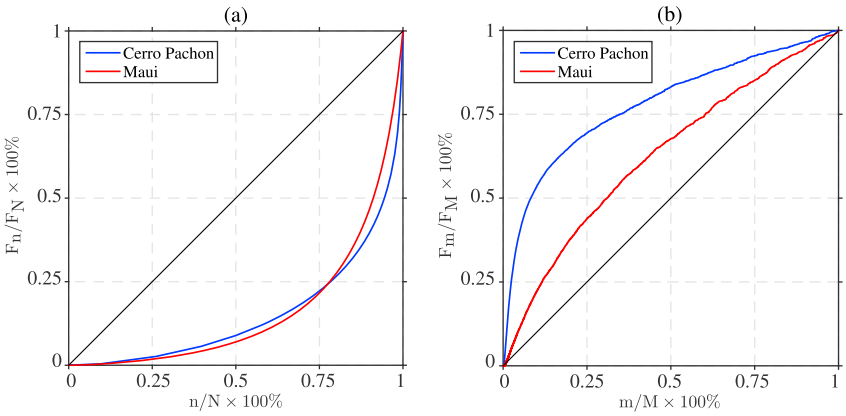

Figure 3. (a) Lorenz curves for Cerro Pachón and Maui. The cumulative sum of number of GWs (n) and MF are normalized to 1. (b) The curve for the cumulative contribution of the waves with MF less than m to the total MF. The magnitudes of MF is normalized by the maximum of $M = 200$ m^2 s^{-2}.

Figure 3b provides a different perspective of this distribution. The cumulative contribution to the total MF is plotted against the magnitudes of GW MF instead of number of waves. A point $(x = m/M, y = F_m/F_M)$ on the plot indicates that *all* waves with MF less than m contribute to y fraction of the total MF. $M = 200$ m^2 s^{-2} is a chosen maximum MF used to normalize the m values. The diagonal line corresponds to the case when the pdf is of the form $f(x) = 1/x$; i.e., the total duration of GWs within a certain MF range is inversely proportional to their MF, so GWs with different MF contribute equally to the total MF. The curves of the two sites are both above the diagonal line, indicating that waves with smaller MF contribute relatively more, because they appear more frequently. The curve for Cerro Pachón is higher than that for Maui, indicating that the contribution from waves with small MF is more significant at Cerro Pachón, consistent with the above analysis with Lorenz curves. For the total MF contributed by GWs with individual MF within 200 m^2 s^{-2}, 50% is from GWs with MF less than 8.5% (32%) of the maximum 200 m^2 s^{-2} at Cerro Pachón (Maui), and 20% is from GWs with MF less than 1.9% (9%) of the maximum at Cerro Pachón (Maui).

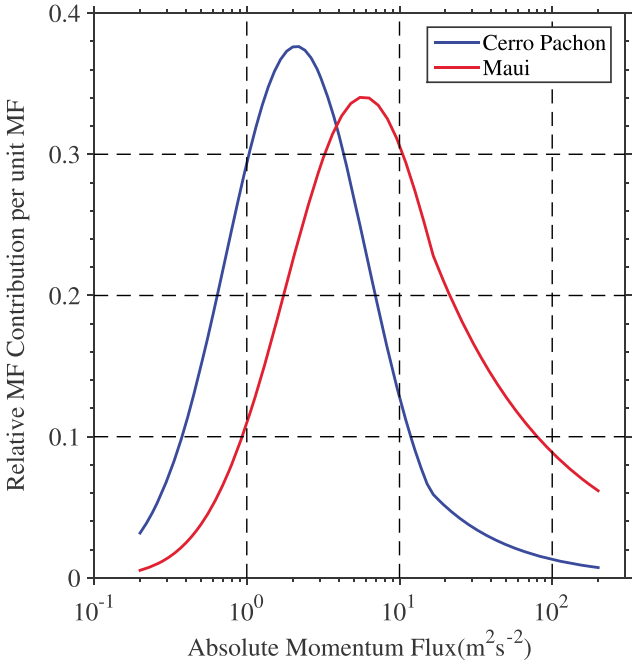

Figure 4. Relative contribution of waves with different MF values to the total MF.

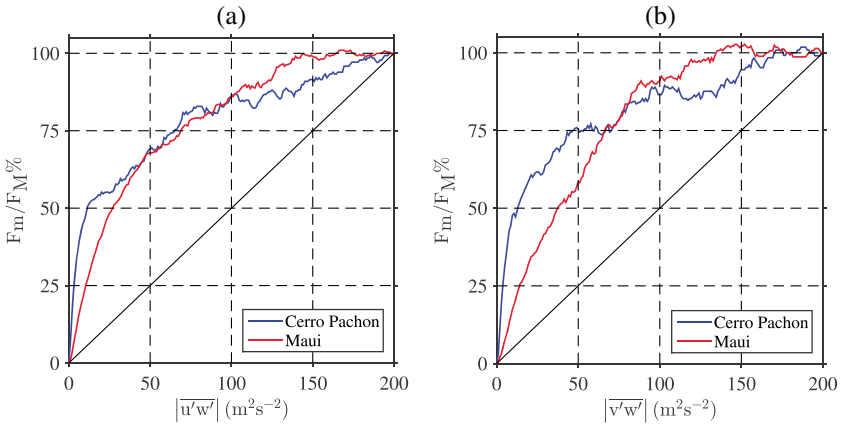

Figure 5. Cumulative contribute to the (a) net zonal and (b) meridional MFs at Cerro Pachón (red) and Maui (blue). A point (m, p) on the curve represents the cumulative contribution to the total MF as a percentage p for waves with MF magnitude less than m. The calculation of MF contribution in each direction takes into account the signs and thus represents the net effect.

The relative contributions can also be quantified by multiplying the GW MF magnitudes with their corresponding probabilities, which yields the relative contributions from GWs of different MF magnitudes per unit MF as shown in Figure 4. This relative contributions compare the comprehensive effects of GWs by considering both the MF magnitude and duration of GWs. These two curves show that the relative contributions follow a near-normal distribution in the semilog coordinates. GWs with large MF do not contribute a lot to the total MF because they appear so infrequently. The most effective GWs have MF values of ~2.2 $m^2\ s^{-2}$ (~5.5 $m^2\ s^{-2}$) at Cerro Pachón (Maui). These values are close to the values of $\exp(\mu)$ discussed in section 3.1.

Finally, a more precise estimate of the total MF should take into account the GW propagation directions. For this purpose, the above analysis was repeated separately for the zonal and meridional MF, $\langle u'w' \rangle$ and $\langle v'w' \rangle$, based on wave propagation directions derived from the airglow image analysis [*Tang et al.*, 2002]. We found that the pdfs of both zonal and meridional MFs (not shown) are very similar to that of the absolute MF at both positive and negative values, with the mean zonal and meridional MFs of 4.39 and 2.44 $m^2\ s^{-2}$ at Maui, and −0.46 and 0.36 $m^2\ s^{-2}$ at Cerro Pachón, respectively. These values are comparable to previous studies [*Li et al.*, 2011; *Gardner and Liu*, 2007] and are very small compared to the MF of those infrequent large waves. Similar to those curves in Figure 3b, the curves for net zonal and meridional MFs are shown in Figure 5. All the curves are still above the diagonal lines, which confirms that the long-term average of MF is contributed more by waves with smaller MF values, and this disparity is more pronounced at Cerro Pachón than at Maui.

3.4. Seasonal Variation

The seasonal variations of the pdfs were obtained by performing the same analysis with data grouped by calendar month from the multiyear data at both sites. The transition points x_0 were fixed for all months using the values in Table 2 to allow a more consistent comparison. The seasonal variations of σ and μ with their 95% confidence levels are shown in Figure 6. Although there are some uncertainties, noticeable annual and semiannual variations can still be found. σ represents the range of variations of MF values for GWs in the lognormal region. At Maui, σ reaches maximum in April and a secondary maximum in December and reaches the minimum in October. At Cerro Pachón, σ is maximum in January with a secondary maximum in April and is at minimum in July. The parameter μ corresponds to the mean MF for GWs in the lognormal region. Its seasonal variations are very similar at both sites, with a strong semiannual variation that peaks in winter and summer. This indicates relatively strong GW activities at these seasons. At Cerro Pachón, the maximum value of μ in winter is much larger than the secondary maximum in summer. This fact matches the results of analyzing the temperature and intensity variances of airglow measurements at El Leoncito (31.8°S, 69.2°W) [*Reisin and Scheer*, 2004], which is very close to ALO.

The seasonal variations of the slope b of the power law distribution are shown in Figure 7. There is a clear annual variation with largest slope in August at Maui and November at Cerro Pachón. The minimum occurs in November at Maui and in March at Cerro Pachón, indicating higher intermittency because the smaller slope

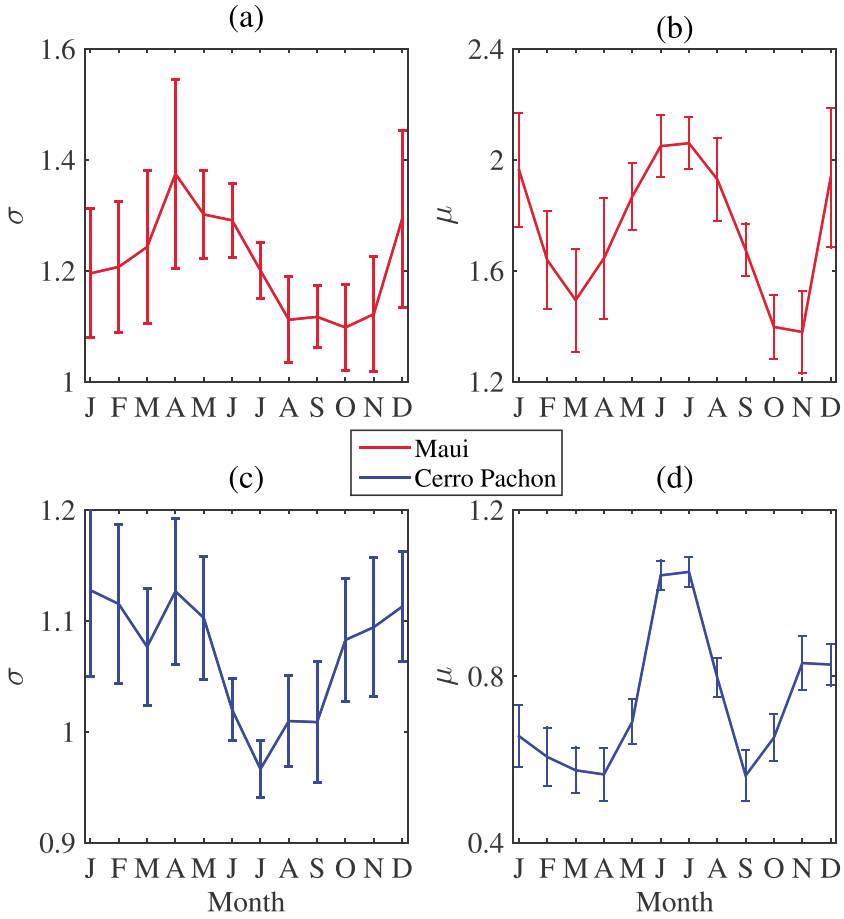

Figure 6. Monthly values of the lognormal parameters (a, c) σ and (b, d) μ of Maui (Figures 6a and 6b) and Cerro Pachón (Figures 6c and 6d), with 95% confidence intervals.

magnitude indicates a broader tail in the power law region. Also shown in Figure 7 are the cumulative probabilities of GWs in the power law region. At both sites, they show a clear semiannual variation, with peaks in winter and summer, indicating relatively more GWs with large MF during these seasons. This also contributes to the larger total MF-like variations of μ as shown in Figures 6b and 6d.

The seasonal variations of the three intermittency parameters are shown in Figure 8. Similar to the earlier analysis with the whole data set, the percentile ratio and the Gini coefficient give consistent measures of the intermittency but the Bernoulli proxy does not. Both the percentile ratio and the Gini coefficient indicate large intermittency around spring and fall and small intermittency in winter and summer. The Gini coefficients are especially consistent at the two sites in different hemispheres: both have the largest intermittency in the fall, the secondary maximum in the spring, and the smallest intermittency in the summer.

In *Hertzog et al.* [2008] the long tails of pdfs progressively disappear from late winter to early summer during their campaign. Similar results are also shown in *Wright et al.* [2013]. This trend corresponds to an increase in the magnitude of *b*, which is also shown in Figure 7 from winter to spring at Maui and from summer to winter at Cerro Pachón. Variations of background wind filtering may be the main reason for this seasonal changes.

4. Discussion

The GW intermittency is mainly influenced by two factors [*Plougonven et al.*, 2013; *Wright et al.*, 2013; *Hertzog et al.*, 2008]. One is the wave source because the physical processes that generate GWs are intermittent. The other is the background atmosphere through which GWs propagate. Fluctuations in the background wind and temperature cause variations in wave filtering, refraction, and dissipation and then influence wave intermittency at the altitudes above. In the lower stratosphere, satellite data [*Wright et al.*, 2013] and balloon data

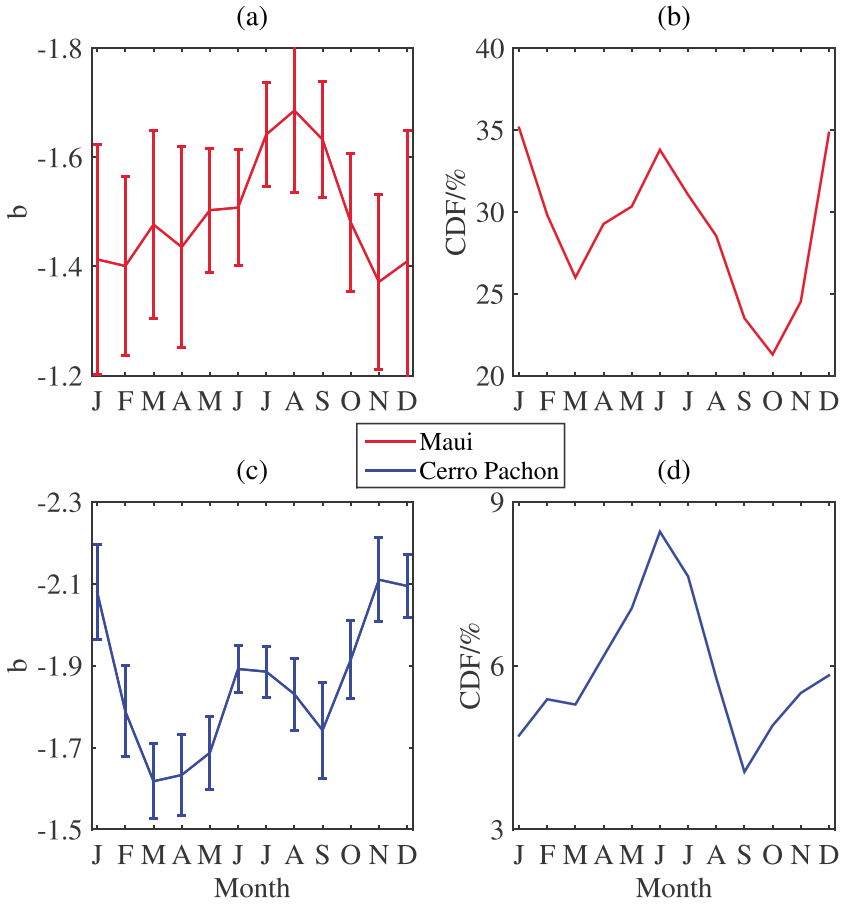

Figure 7. Seasonal variations of the power law parameters *b* at (a) Maui and (c) Cerro Pachón, with 95% confidence intervals, and the cumulative probability of the power law region at (b) Maui and (d) Cerro Pachón.

[*Plougonven et al.*, 2013] both show that orographically excited GWs always show higher intermittency, as indicated by larger Gini coefficient and broader tails in pdfs of MF. Since the lower stratosphere is close to the GW source, these results imply that the source intermittency is generally higher for orographic GWs. The mesopause region is much farther away from GW sources, and it is expected that the background fluctuations play more important roles in affecting the GW intermittency in this region. The higher intermittency at Maui is likely due to higher variability of the background atmosphere, because Maui is not expected to have a higher number of orographic GWs as Cerro Pachón. The consistency in seasonal variation of intermittency at the two sites is another evidence of strong influence of background atmosphere.

When comparing intermittency among different measurements, it is important to note that different instruments are sensitive to different parts of the spatial and temporal spectra of GWs. The effects of "observation filter" [*Alexander*, 1998; *Alexander et al.*, 2010] should be carefully considered. As shown in Figure 8a in *Alexander et al.* [2010], satellite (infrared limb sounding) and superpressure balloons have different visibilities to the GW spectrum. The airglow images are sensitive to waves with relatively large vertical wavelength (>10 km) and short horizontal wavelength (approximately tens of kilometers) [*Li et al.*, 2011], which covers the part of the spectrum that is "invisible" to satellite limb sounding and balloons. Even though this observation filter may potentially affect the pdfs of detected GWs, the remarkable similarities between pdfs in this study and those obtained with different instruments strongly suggest that the lognormal and power law distributions are universal features across the entire GW spectrum.

In the airglow imager data analysis, one consequence of using TD image is that it removes all stationary mountain waves. The mountain waves can be an important source of MF, especially above Cerro Pachón during austral winter. However, only mountain waves generated by steady surface wind propagating in a steady background atmosphere are stationary. Many orographically generated GWs are transient or intermittent due

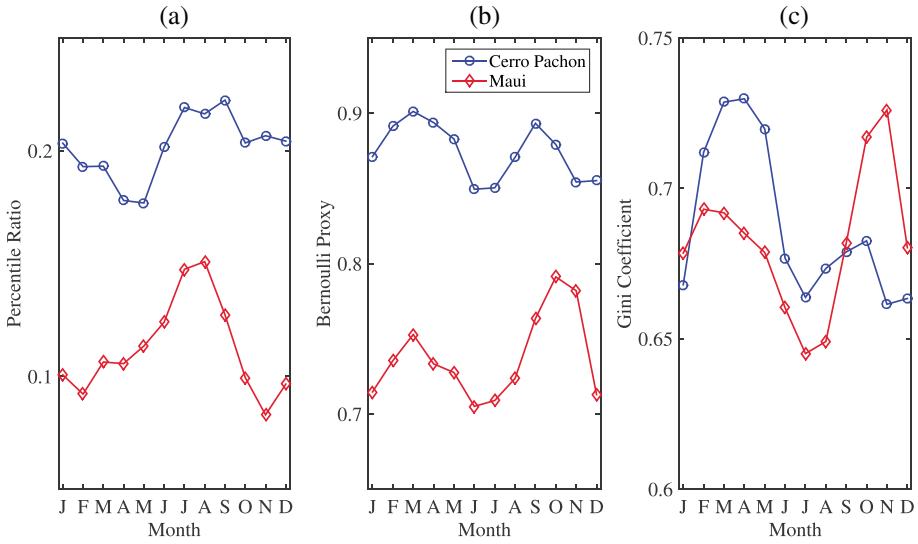

Figure 8. Seasonal variations of the intermittency at Maui (red) and Cerro Pachón (blue) as measured by (a) the percentile ratio, (b) the Bernoulli proxy, and (c) the Gini coefficient. Large intermittency corresponds to small values in percentile ratio and Bernoulli proxy but large values in Gini coefficient.

to surface wind intermittency or changing background atmosphere and can be detected with our analysis method and are included in the pdfs. Small-amplitude, stationary mountain waves are very difficult to detect, because they are often not steady enough over a long time to be identified. If detectable stationary mountain waves are included, we expect that they may contribute to a little increase of the pdf in the large MF region but will not significantly alter the current results.

We should also point out that the impact of GWs on the background atmosphere is related to the MF, but the net forcing is dependent on the momentum deposition from dissipating GWs. Nondissipating GWs transport momentum but do not impart a net forcing to the background atmosphere. The data from a single layer of airglow cannot provide vertical variation of MF; therefore, it is inadequate for directly calculating momentum deposition. In addition, if GWs are ducted under certain conditions, they can propagate both upward and downward in a layer with a zero net MF. Many observational studies on wave ducting [*Isler et al.*, 1997; *Walterscheid et al.*, 1999; *Hecht et al.*, 2001; *Ejiri et al.*, 2003; *Nielsen et al.*, 2009] suggest that the ducted GWs are highly variable and the percentages of ducted waves vary from a few percent to over 70%. Nevertheless, the mesopause region is where most GWs break and deposit their momentum; the statistics of the absolute MF presented here is a good proxy of the overall impact of GWs. A more detailed study of GW forcing should take into account wave dissipation and ducting, with additional measurements of airglow from different altitudes or data from other instruments, to resolve the vertical variation of MF.

5. Conclusion

We have obtained for the first time the probability density functions (pdfs) of GW MF in the mesopause region at Maui and Cerro Pachón, based on multiyear airglow image data. The pdfs for GWs with smaller MF are found to fit very well with a lognormal distribution. The pdfs in the larger MF region, described as "long tail" in *Hertzog et al.* [2012], fit very well with a power law distribution. The transition points between the two different distributions are around $\sim$16 m^2 s^{-2} at both sites. Because of the large amount of GWs, these two distributions are well defined through the fitting process. It enables a detailed study of GW intermittency and their relative contributions to the total MF.

The GW intermittency was quantified using three parameters: the Bernoulli proxy, the percentile ratio, and the Gini coefficient. The first two parameters show that GWs have higher intermittency at Maui than at Cerro Pachón, while the Gini coefficient shows little difference between the two sites. Monte Carlo simulations were performed to examine the relationships of the pdf with the three intermittency parameters and revealed some inconsistencies. The same change of the pdf parameters may result in opposite change in intermittency measured with three different parameters. This shows the limitations of using these parameters in representing

GW intermittency. In general, the percentile ratio and the Gini coefficient give more consistent intermittency measure than the Bernoulli proxy.

Even with these inconsistencies, it is clear that the overall intermittency is much larger at Maui. Mesopause region is farther away from the wave sources. Assuming the source intermittency is larger for orographic GWs, as shown in previous studies in the stratosphere, the observed larger intermittency at Maui is indicative of a larger background variability at this site.

We also examined the relative importance of GWs in terms of their contribution to the total MF. If measured in terms of the overall time and number of waves, the majority of the total MF is contributed by a small fraction of GWs with largest MF. At both sites, during 22% of the time GWs with largest MF contribute to 75% of the total MF. However, if measured in terms of MF values, those with small MF contribute relatively more. GWs with MF less than 8.5% (32%) of the maximum MF (200 $m^2\ s^{-2}$) contribute to 50% of the total MF at Cerro Pachón (Maui). In terms of the relative contributions at different MF values, GWs with MF around 2.2 $m^2\ s^{-2}$ at Cerro Pachón and 5.5 $m^2\ s^{-2}$ at Maui are most effective contributors.

Seasonal variations of the pdfs and intermittency are also examined. Clear annual and semiannual variations are found and are remarkably consistent at the two sites. By comparing the Gini coefficient at both sites, we found that the largest intermittency is in the fall, with a secondary maximum in the spring. The minimum intermittency occurs in summer and the secondary minimum is in winter. Because of the different characteristics of the GW sources at the two sites, the consistency in seasonal variation is another evidence that the intermittency in the mesopause region is largely determined by the GW propagation conditions associated with the background atmosphere.

This work provided a new perspective to the GW characteristics in the mesopause region using existing airglow measurements. GWs are known to vary significantly at different geographical locations [e.g., *Espy et al.*, 2004]. With many airglow imager observations around the world, the global distribution of GW intermittency can be derived and used to validate GCM representations of GWs.

Acknowledgments
The data and program used in this analysis are available upon request (caob@my.erau.edu). The authors thank the reviewers for their valuable suggestions on this paper, which result in significant improvement. This work is supported by NSF grants AGS-1110199 and AGS-1115249 and NSFC grant 41274154. The Andes Lidar Observatory is part of the Consortium of Resonance Rayleigh Lidars, supported by NSF grants AGS-1136278 and AGS-1136208. We are grateful for the excellent support of the ALO facility provided by the Association of Universities for Research in Astronomy.

References

Alexander, M. J. (1998), Interpretations of observed climatological patterns in stratospheric gravity wave variance, *J. Geophys. Res.*, *103*(D8), 8627–8640, doi:10.1029/97JD03325.

Alexander, M. J., and T. J. Dunkerton (1999), A spectral parameterization of mean-flow forcing due to breaking gravity waves, *J. Atmos. Sci.*, *56*(24), 4167–4182.

Alexander, M. J., and A. W. Grimsdell (2013), Seasonal cycle of orographic gravity wave occurrence above small islands in the southern hemisphere: Implications for effects on the general circulation, *J. Geophys. Res. Atmos.*, *118*, 11,589–11,599, doi:10.1002/2013JD020526.

Alexander, M. J., J. R. Holton, and D. Durran (1995), The gravity wave response above deep convection in squall line simulation, *J. Atmos. Sci.*, *52*(12), 2212–2226.

Alexander, M. J., P. T. May, and J. H. Beres (2004), Gravity waves generated by convection in the Darwin area during the Darwin Area Wave Experiment, *J. Geophys. Res.*, *109*, D20S04, doi:10.1029/2004JD004729.

Alexander, M. J., et al. (2010), Recent developments in gravity-wave effects in climate models and the global distribution of gravity-wave momentum flux from observations and models, *Q. J. R. Meteorol. Soc.*, *136*(650), 1103–1124, doi:10.1002/qj.637.

Andrews, D. G., J. R. Holton, and C. B. Leovy (1987), *Middle Atmosphere Dynamics*, vol. 40, Academic Press, New York.

Beres, J. H., R. R. Garcia, B. A. Boville, and F. Sassi (2005), Implementation of a gravity wave source spectrum parameterization dependent on the properties of convection in the Whole Atmosphere Community Climate Model (WACCM), *J. Geophys. Res.*, *110*, D10108, doi:10.1029/2004JD005504.

Butchart, N. (2014), The Brewer-Dobson circulation, *Rev. Geophys.*, *52*(2), 157–184, doi:10.1002/2013RG000448.

Cohen, N. Y., E. P. Gerber, and O. Bühler (2014), What drives the Brewer–Dobson circulation?, *J. Atmos. Sci.*, *71*(10), 3837–3855, doi:10.1175/JAS-D-14-0021.1.

Ejiri, M. K., K. Shiokawa, T. Ogawa, K. Igarashi, T. Nakamura, and T. Tsuda (2003), Statistical study of short-period gravity waves in OH and OI nightglow images at two separated sites, *J. Geophys. Res.*, *108*(D21), 4679, doi:10.1029/2002JD002795.

Espy, P. J., G. O. L. Jones, G. R. Swenson, J. Tang, and M. J. Taylor (2004), Tidal modulation of the gravity-wave momentum flux in the Antarctic mesosphere, *Geophys. Res. Lett.*, *31*, L11111, doi:10.1029/2004GL019624.

Franke, S. J., X. Chu, A. Z. Liu, and W. K. Hocking (2005), Comparison of meteor radar and Na Doppler lidar measurements of winds in the mesopause region above Maui, Hawaii, *J. Geophys. Res.*, *110*(D9), D09S02, doi:10.1029/2003JD004486.

Fritts, D. C., and M. J. Alexander (2003), Gravity wave dynamics and effects in the middle atmosphere, *Rev. Geophys.*, *41*(1), 1003, doi:10.1029/2001RG000106.

Fritts, D. C., and R. A. Vincent (1987), Mesospheric momentum flux studies at Adelaide, Australia: Observations and a gravity wave–tidal interaction model, *J. Atmos. Sci.*, *44*(3), 605–619.

Fritts, D. C., L. Wang, J. A. Werne, T. Lund, and K. Wan (2009), Gravity wave instability dynamics at high Reynolds numbers. Part I: Wave field evolution at large amplitudes and high frequencies, *J. Atmos. Sci.*, *66*(5), 1126–1148.

Gardner, C. S., and A. Z. Liu (2007), Seasonal variations of the vertical fluxes of heat and horizontal momentum in the mesopause region at Starfire Optical Range, New Mexico, *J. Geophys. Res.*, *112*, D09113, doi:10.1029/2005JD006179.

Gierasch, P., R. Goody, and P. Stone (1970), The energy balance of planetary atmospheres, *Geophys. Fluid Dyn.*, *1*, 1–18.

Hecht, J. H., R. L. Walterscheid, M. P. Hickey, and S. J. Franke (2001), Climatology and modeling of quasi-monochromatic atmospheric gravity waves observed over Urbana, Illinois, *J. Geophys. Res.*, *106*(D6), 5181–5195, doi:10.1029/2000JD900722.

Hertzog, A., G. Boccara, R. A. Vincent, F. Vial, and P. Cocquerez (2008), Estimation of gravity wave momentum flux and phase speeds from quasi-Lagrangian stratospheric balloon flights. Part II: Results from the Vorcore campaign in Antarctica, *J. Atmos. Sci.*, *65*(10), 3056–3070.

Hertzog, A., M. J. Alexander, and R. Plougonven (2012), On the intermittency of gravity wave momentum flux in the stratosphere, *J. Atmos. Sci.*, *69*(11), 3433–3448.

Holton, J. R. (1982), The role of gravity wave induced drag and diffusion in the momentum budget of the mesosphere, *J. Atmos. Sci.*, *39*(4), 791–799.

Isler, J. R., M. J. Taylor, and D. C. Fritts (1997), Observational evidence of wave ducting and evanescence in the mesosphere, *J. Geophys. Res.*, *102*(D22), 26,301–26,313, doi:10.1029/97JD01783.

Jewtoukoff, V., R. Plougonven, and A. Hertzog (2013), Gravity waves generated by deep tropical convection: Estimates from balloon observations and mesoscale simulations, *J. Geophys. Res. Atmos.*, *118*, 9690–9707, doi:10.1002/jgrd.50781.

Li, F., G. R. Swenson, A. Z. Liu, M. J. Taylor, and Y. Zhao (2007), Investigation of a "wall" wave event, *J. Geophys. Res.*, *112*, D04104, doi:10.1029/2006JD007213.

Li, Z., A. Z. Liu, X. Lu, G. R. Swenson, and S. J. Franke (2011), Gravity wave characteristics from OH airglow imager over Maui, *J. Geophys. Res.*, *116*, D22115, doi:10.1029/2011JD015870.

Li, Z., A. Z. Liu, and G. G. Sivjee (2014), Removing Milky Way from airglow images using principal component analysis, *J. Atmos. Sol. Terr. Phys.*, *110–111*, 50–57, doi:10.1016/j.jastp.2014.01.016.

Lindzen, R. S. (1981), Turbulence and stress owing to gravity wave and tidal breakdown, *J. Geophys. Res.*, *86*(C10), 9707–9714, doi:10.1029/JC086iC10p09707.

Liou, K.-N. (2002), *An Introduction to Atmospheric Radiation*, *Int. Geophys. Ser.*, vol. 84, 2nd ed., Academic Press, San Diego, Calif.

Liu, A. Z., and G. R. Swenson (2003), A modeling study of O_2 and OH airglow perturbations induced by atmospheric gravity waves, *J. Geophys. Res.*, *108*(D4), 4151, doi:10.1029/2002JD002474.

Lorenz, M. O. (1905), Methods of measuring the concentration of wealth, *Publ. Am. Stat. Assoc.*, *9*(70), 209–219.

Nielsen, K., M. J. Taylor, R. E. Hibbins, and M. J. Jarvis (2009), Climatology of short-period mesospheric gravity waves over Halley, Antarctica (76°S, 27°W), *J. Atmos. Sol. Terr. Phys.*, *71*(8–9), 991–1000, doi:10.1016/j.jastp.2009.04.005.

Picone, J. M., A. E. Hedin, and D. Drob (2002), NRLMSISE-00 empirical model of the atmosphere: Statistical comparisons and scientific issues, *J. Geophys. Res.*, *107*(A12), 1468, doi:10.1029/2002JA009430.

Plougonven, R., A. Hertzog, and L. Guez (2013), Gravity waves over Antarctica and the Southern Ocean: Consistent momentum fluxes in mesoscale simulations and stratospheric balloon observations, *Q. J. R. Meteorol. Soc.*, *139*(670), 101–118, doi:10.1002/qj.1965.

Reisin, E. R., and J. Scheer (2004), Gravity wave activity in the mesopause region from airglow measurements at El Leoncito, *J. Atmos. Sol. Terr. Phys.*, *66*(6–9), 655–661, doi:10.1016/j.jastp.2004.01.017.

Richter, J. H., F. Sassi, and R. R. Garcia (2010), Toward a physically based gravity wave source parameterization in a general circulation model, *J. Atmos. Sci.*, *67*, 136–156, doi:10.1175/2009JAS3112.1.

Snively, J. B., and V. P. Pasko (2003), Breaking of thunderstorm-generated gravity waves as a source of short-period ducted waves at mesopause altitudes, *Geophys. Res. Lett.*, *30*(24), 2254, doi:10.1029/2003GL018436.

Suzuki, S., K. Shiokawa, A. Z. Liu, Y. Otsuka, T. Ogawa, and T. Nakamura (2009), Characteristics of equatorial gravity waves derived from mesospheric airglow imaging observations, *Ann. Geophys.*, *27*, 1625–1629, doi:10.5194/angeo-27-1625-2009.

Swenson, G. R., and C. S. Gardner (1998), Analytical models for the responses of the mesospheric OH* and Na layers to atmospheric gravity waves, *J. Geophys. Res.*, *103*(D6), 6271–6294, doi:10.1029/97JD02985.

Tang, J., A. Z. Liu, and G. R. Swenson (2002), High frequency gravity waves observed in OH airglow at Starfire Optical Range, NM: Seasonal variations in momentum flux, *Geophys. Res. Lett.*, *29*(20), 1966, doi:10.1029/2002GL015794.

Tang, J., F. Kamalabadi, S. J. Franke, A. Z. Liu, and G. R. Swenson (2005a), Estimation of gravity wave momentum flux using spectroscopic imaging, *IEEE Trans. Geosci. Remote Sens.*, *43*(1), 103–109.

Tang, J., S. J. Franke, F. Kamalabadi, and G. R. Swenson (2005b), Motion extraction of atmospheric waves from spectroscopic imaging, *IEEE Geosci. Remote Sens. Lett.*, *2*(2), 229–232.

Tang, J., G. R. Swenson, A. Z. Liu, and F. Kamalabadi (2005c), Observational investigations of high frequency gravity wave momentum flux with airglow imaging, *J. Geophys. Res.*, *110*, D09S09, doi:10.1029/2004JD004778.

Vadas, S. L., D. C. Fritts, and M. J. Alexander (2003), Mechanism for the generation of secondary waves in wave breaking regions, *J. Atmos. Sci.*, *60*(1), 194–214.

Walterscheid, R. L., J. H. Hecht, R. A. Vincent, I. M. Reid, J. Woithe, and M. P. Hickey (1999), Analysis and interpretation of airglow and radar observations of quasi-monochromatic gravity waves in the upper mesosphere and lower thermosphere over Adelaide, Australia (35°S, 138°E), *J. Atmos. Sol. Terr. Phys.*, *61*, 461–478, doi:10.1016/S1364-6826(99)00002-4.

Wright, C. J., S. M. Osprey, and J. C. Gille (2013), Global observations of gravity wave intermittency and its impact on the observed momentum flux morphology, *J. Geophys. Res. Atmos.*, *118*, 10,980–10,993, doi:10.1002/jgrd.50869.